Appl. Phys. A 68, 615–625 (1999) / DOI 10.1007/s003399900051

Applied Physics A
Materials
Science & Processing

Invited paper

Model for laser-induced thermal degradation and ablation of polymers

N. Arnold*, **N. Bityurin****

Angewandte Physik, Johannes-Kepler-Universität, Altenbergerstraße 69, A-4040, Linz, Austria
(Fax: +43-732/2468-9242, E-mail: nikita.arnold@jk.uni-linz.ac.at)

Received: 16 February 1999/Accepted: 18 February 1999/Published online: 28 April 1999

Abstract. Ablation of organic polymers is described on the basis of photothermal bond breaking within the bulk material. Here, we assume a first-order chemical reaction, which can be described by an Arrhenius law. Ablation starts when the density of broken bonds at the surface reaches a certain critical value.

In order to understand the ablation behavior near the threshold fluence, ϕ_{th}, *non-stationary* regimes must be considered. The present treatment reveals several qualitative differences with respect to models that treat ablation as a *surface* process: (i) Ablation starts sharply with a front velocity that has its maximum value just after the onset. (ii) The transition to the quasi-stationary ablation regime is faster. (iii) Near threshold, the ablated depth h has a square-root dependence on laser fluence, i.e., $h \propto (\phi - \phi_{\mathrm{th}})^{1/2}$. The ablation velocity is very high even near ϕ_{th}. (iv) With $\phi \approx \phi_{\mathrm{th}}$ ablation starts well after the laser pulse. (v) The depletion of species is responsible for the Arrhenius tail observed with fluences $\phi \leq \phi_{\mathrm{th}}$. (vi) Residual modification of material has maximum near the threshold. (vii) *Stationary* regimes of ablation demonstrate change of effective activation energy with laser intensity.

The model calculations are applied to Polyimide (Kapton$^{\mathrm{TM}}$ H). Here, differences in single-pulse ablated depth determined from mass loss and profilometry should be about 10 nm.

PACS: 82.65; 82.50; 42.10; 81.15.Fg

The physical and chemical mechanisms involved in the UV-laser ablation of polymers [1, 2] are still under discussion. It is generally agreed that in ns pulses in a primary step the energy of photons is transformed into the energy of electronic excitation. However, subsequent steps in the ablation process may be quite different [3].

Let us first enumerate experimental facts, which motivate further theoretical considerations. It is well-known that ablation rates are measured by different techniques that yield non-equivalent results, in particular near the threshold fluence for ablation ϕ_{th}:

- The ablated depth measured by profilometry (optical interferometer, mechanical stylus [4], atomic force microscope (AFM) [5]) starts *sharply* at fluence $\phi = \phi_{\mathrm{th}}$ (Fig. 1a). Similar conclusions can be drawn from reflectivity [6] or acoustic response measurements [7].
- The ablation rate recalculated from mass loss measurements using a quartz crystal microbalance (QCM) [8] or mass spectrometry reveals an Arrhenius tail (Fig. 1b).
- Ablation is frequently accompanied by chemical and/or physical modification of material within a certain depth. With Polyimide (PI), for example, changes in the electrical conductivity [9], optical transmission [10, 11], and composition [12, 13] have been observed.

Different models were applied for the description of UV-laser ablation of polymers. One can distinguish between the *photochemical* models [14–19], where electronic excitation results in direct bond breaking (without thermalization), and models, where the bonds are *thermally* broken [20–27]. Thermal nature of the ablation process is supported by the observation of Arrhenius tails [8], the dependence of the ablation rate and threshold on the laser pulse repetition rate [28], and pulse length [5, 25, 29].

For *photophysical* models both thermal and non-thermal features are important. They consider either two independent channels of bond breaking [30, 31], or imply different bond breaking energies for ground state and electronically excited chromophores [32, 33]. Such mechanisms may be important for ps and fs laser pulses [25, 34].

From another perspective, the present models can be subdivided into *volume* and *surface* models. With surface models the processes responsible for material removal take place only within several monolayers from the surface. As a result, the velocity of the interface between the gaseous and condensed phase depends explicitly only on the *surface* temperature

* Corresponding author.
** On leave from: Institute of Applied Physics RAS, Nizhnii Novgorod, Russia

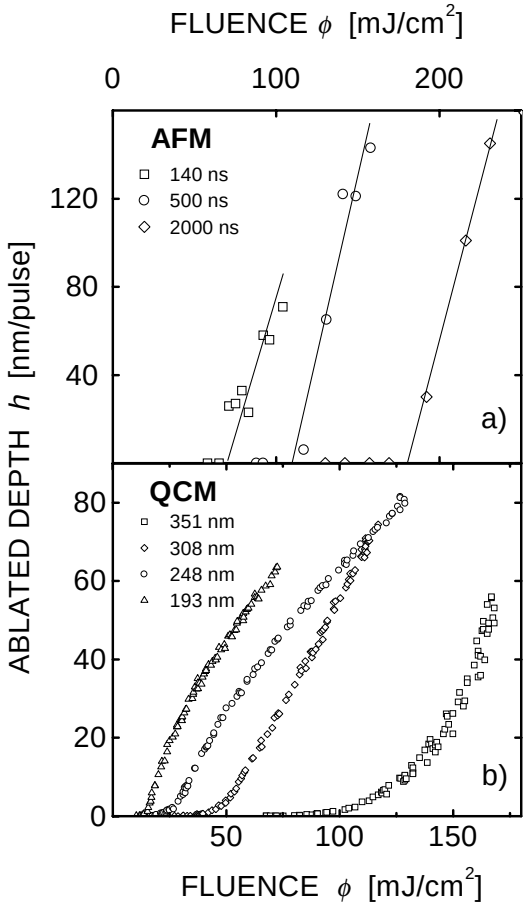

Fig. 1a,b. Differences in ablated depth vs. laser fluence curves near single-pulse ablation threshold for PI Kapton^{TM} H. **a** Profile measurements performed by AFM demonstrate sharp threshold [5] (Ar^+ laser $\lambda \approx 302$ nm). Different sets of data show results for different pulse duration (with constant intensity). *Lines* are guides for the eye. **b** Mass-loss measurements performed with QCM for different wavelengths show Arrhenius tails [8]

or laser-light intensity. With volume models, the processes, which lead to the decomposition of material, take place *within the bulk* material.

The volume and surface models investigated up to now include:

– *Photochemical surface* models [35]. These seem to be irrelevant in ns laser ablation, as corresponding processes require longer interaction times and/or higher doses of laser radiation.
– *Photochemical volume* models as considered in [14–18, 36] reveal a *sharp* ablation threshold and lead to a logarithmic dependence of the ablated depth per pulse, h:

$$h = \alpha^{-1} \ln(\phi/\phi_{\rm th}) \,, \tag{1}$$

where α is the absorption coefficient. Such models may also result in a linear dependence $h(\phi)$, if the movement of the ablation front is taken into account, and if the screening by ablation products is ignored. They *do not*, however, explain the Arrhenius tails observed in mass loss measurements.
– *Thermal surface* models [23, 25, 26, 32, 37], (developed in connection with the laser ablation of metals [38, 39] do reveal a *smooth* Arrhenius-type ablation onset, due to the Arrhenius dependence of the recession velocity on temperature:

$$v = \nu_0 \exp(-T_{\rm a}/T_{\rm s}) \,. \tag{2}$$

Such models *do not*, however, describe sharp ablation threshold observed with polymers in profile measurements.
– *Thermal volume* models are often oversimplified [8, 20], they frequently ignore the influence of the moving boundary on the heat equation [22, 24], which resulted in unrealistically high temperatures. Besides, in the reported examples, they do not explain Arrhenius tails, thus losing one of the main advantages of thermal models.

Thus, it looks attractive to combine volume features of photochemical models and thermal features of surface models in a single approach. The processes should be thermal, which shall explain Arrhenius tails. The bulk nature of the decomposition process shall describe sharp onset of ablation.

One comment is in place here. The modeling of depth-fluence ablation curves at *high* fluences is not sensitive to the underlying mechanisms of ablation itself. At such fluences ablation rate is mainly determined by the screening of the radiation by the ablated products [26, 31]. This leads to some type of logarithmic dependence $h(\phi)$ [26, 40, 41]. For deeper understanding of the mechanism of ablation, we shall place emphasis on the near-threshold behavior, where screening is unimportant.

The goal of the present article is to study the functional relationships, which follow from the volume decomposition model, and to emphasize its similarities to, and distinctions from, the surface models.

1 Model

A schematic picture of the model is shown in Fig. 2. Light absorption follows Beer's law:

$$\frac{\partial I}{\partial x} = -\alpha I \,. \tag{3}$$

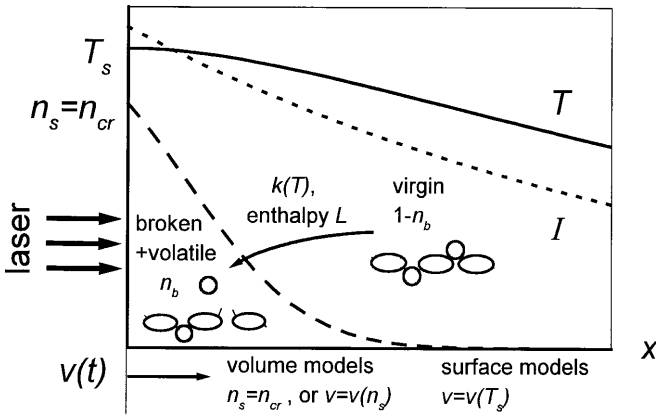

Fig. 2. Schematic of the model. Intensity I (*dotted line*) creates temperature distribution T within the material (*solid line*). Thermal bond breaking with the rate $k(T)$ and negative heat effect L takes place within the volume. It produces the distribution of broken bonds $n_{\rm b}$ and may create volatile species trapped within the polymer matrix. Position of the interface is determined by the surface concentration $n_{\rm s} \equiv n_{\rm b}(x = 0)$, as opposed to surface models, where it depends on the surface temperature $T_{\rm s} \equiv T(x = 0)$

The electronic excitations thermalize on a ps time scale [42]. Heating is described by the one-dimensional heat equation. Subsequently we employ a moving reference frame, which is fixed with the ablation front.

$$\frac{\partial H}{\partial t} = \nu \frac{\partial H}{\partial x} + \frac{\partial}{\partial x}\left(K \frac{\partial T}{\partial x}\right) - \frac{\partial I}{\partial x} - L(1-n_\mathrm{b}) k_0 \exp(-T_\mathrm{a}/T). \tag{4}$$

Here T is the temperature, K the thermal conductivity,

$$H = \rho \int_{T_0}^{T} c(T')\,\mathrm{d}(T') \,, \tag{5}$$

is the volumetric enthalpy with c being the specific heat, ρ (constant) polymer density, and T_0 the ambient temperature. The last (Arrhenius) term describes thermally activated first-order bond breaking within the bulk material: $1-n_\mathrm{b} \overset{k(T)}{\rightarrow} n_\mathrm{b}$. n_b is the fraction of "broken" bonds per unit volume, $1-n_\mathrm{b}$ is the fraction of "virgin" bonds. $L \equiv \Delta H_\mathrm{b} N_0$ is the enthalpy per unit volume required to break all bonds; $L > 0$ for endothermic reactions. ΔH_b is the enthalpy per bond and N_0 total (initial) number density of bonds. The equation of chemical kinetics is

$$\frac{\partial n_\mathrm{b}}{\partial t} = \nu \frac{\partial n_\mathrm{b}}{\partial x} + (1-n_\mathrm{b}) k_0 \exp(-T_\mathrm{a}/T) \,, \tag{6}$$

where k_0 is a pre-exponential factor.

Equations (4) and (6) are coupled via the velocity ν. We assume that material is ablated when the number of broken bonds at the surface reaches a critical value. Thus, the interface between the gaseous and the condensed phase is determined by the requirement:

$$n_\mathrm{b}|_{x=0} = n_\mathrm{cr} \,. \tag{7a}$$

This relation defines the position of the interface, and therefore the velocity ν, implicitly. Another possibility is to define

$$\nu = \nu(n_\mathrm{b}|_{x=0}) \,, \tag{7b}$$

where the function ν in the r.h.s. should be derived from microscopic considerations. The difference between (7a) and (7b) is similar to that between Stefan and Frenkel–Wilson formulations for the velocity of the melting front [3]. If $\nu(n_\mathrm{b}(0))$ in (7b) sharply increases from zero at $n_\mathrm{b}(0) \approx n_\mathrm{cr}$, (7b) becomes identical to (7a). Thus, definition (7b) is more general, and (7a) is its limiting case.

The physical meaning of the interface between gaseous and condensed phase is that the value of thermal conductivity K drops sharply across this interface, and the heat flux through the interface can be neglected.

$$-K \left.\frac{\partial T}{\partial x}\right|_{x=0} = 0 \,. \tag{8}$$

The boundary conditions at infinity are obvious:

$$T|_{x\to\infty} = T_0 \,, \quad n_\mathrm{b}|_{x\to\infty} = 0 \,. \tag{9}$$

We emphasize here the conceptual similarities and differences between the present *thermal bulk* model and *thermal surface* models developed for laser ablation of metals [38, 39] and successfully applied to laser ablation of polymers [23, 25, 26, 32]. Both models are purely thermal and use the 1-D heat equation to calculate the temperature distribution. The movement of the interface must be taken into account. In the volume model the velocity is determined by the concentration of bonds at the surface, which requires solution of the equation of chemical kinetics (6). The Arrhenius factor in this equation depends on the temperature distribution within the material. Thus, we consider layer by layer material removal, but it results from the volume decomposition of the polymer.

In thermal surface models the rate of evaporation is proportional to the saturated vapor pressure and (6) and (7) are replaced by the single expression (2). The Arrhenius factor in this expression depends only on the surface temperature, i.e., it assumes bond breaking only at the surface.

Another difference concerns the ablation enthalpy. With volume models it enters as a sink in the heat equation (4), whereas with surface models it transforms the boundary condition (8) into (see [39] for more details):

$$-K \left.\frac{\partial T}{\partial x}\right|_{x=0} = -\nu L \,. \tag{10}$$

These distinctions lead to several qualitative differences between the predictions of both models.

The most important factors not included into consideration at this stage are: (i) no backward and/or subsequent chemical reaction is assumed, (ii) material properties do not depend on chemical changes, (iii) screening of radiation by the ablated products is ignored.

These factors can be easily incorporated. However, our goal is to study the thermal volume decomposition model in its simplest formulation, to perceive its similarities and distinctions from the surface ablation models, and to obtain the main predictions, which follow from such a model.

2 Stationary thermal volume decomposition wave

In laser ablation, the understanding of the stationary regime of material removal (with constant incident intensity I and recession velocity ν) is prerequisite for further studies. Its consideration for surface models allows one to understand many features of the laser ablation of metals. We considered stationary ablation within the model of Sect. 1 (with zero ablation enthalpy $L = 0$) in [27] Here, we generalize the results to $L \neq 0$ and introduce concepts and notations, that will be subsequently used. In general, the stationary velocity of the interface is determined by the energy conservation, and the temperature is such that the Arrhenius reaction rate is fast enough to maintain this velocity. As a result, velocity is about linear with intensity, while (surface) temperature depends logarithmically on I in almost every thermal model. Subsequent mathematical analysis reveals, however, some differences between the surface and volume models.

It is convenient to introduce a (positive) quantity b, which monotonously increases with n_b.

$$b \equiv -\ln(1-n_\mathrm{b}) \,. \tag{11}$$

With this notation (6) can be rewritten the simpler form:

$$\frac{\partial b}{\partial t} = \nu \frac{\partial b}{\partial x} + k \,. \tag{12}$$

We will often employ the saddle point approximation for the reaction rate. It uses Taylor expansion of T near the surface under the assumption $T_a/T_s \gg 1$.

$$k \equiv k_0 \exp(-T_a/T) \approx k_s \exp(-x^2/l_k^2) \,, \tag{13}$$

$$k_s \equiv k_0 \exp(-T_a/T_s) \,, \quad l_k \equiv l(T_s/T_a)^{1/2} \,,$$

$$l^2 \equiv -2T_s \Big/ \left.\frac{\partial^2 T}{\partial x^2}\right|_{x=0} \,. \tag{14}$$

Henceforth index "s" refers to the quantities at the surface $x = 0$. l_k characterizes the width of the reaction region, and l is spatial width of the temperature distribution. The zero-flux boundary condition (8) allows us to find $\partial^2 T/\partial x^2 (x = 0)$ from the heat equation:

$$c_s \rho \dot{T}_s = K_s \left.\frac{\partial^2 T}{\partial x^2}\right|_{x=0} + \alpha I_s - L(1-n_s)k_s \,. \tag{15}$$

In the stationary regime integrating (12) over x we can relate velocity ν and temperature distribution:

$$\nu b_s = \int_0^\infty k \, \mathrm{d}x \approx \frac{\sqrt{\pi}}{2} l_k k_s \,. \tag{16}$$

The last equality assumes the approximate expression (13) for the Arrhenius reaction rate k in (12). This makes the dependence on *surface* temperature dominant, resembling surface models. Note however, that the width of reaction zone l_k depends on I_s via (14) and (15).

One more relation between T_s and ν is provided by the heat equation. It is convenient to combine the reaction enthalpy and the heating enthalpy using (6):

$$\left[\frac{\partial}{\partial t} - \nu \frac{\partial}{\partial x}\right][H + L n_b] = \frac{\partial}{\partial x}\left(K \frac{\partial T}{\partial x}\right) - \frac{\partial I}{\partial x} \,. \tag{17}$$

Integrating this over x in the stationary case with (8) one obtains energy conservation:

$$\nu [H_s + L n_s] = I_s \,. \tag{18}$$

Equations (16) and (18) define stationary ν and T_s. In all subsequent expressions for Stefan-type boundary condition (7a) n_{cr} should be used in place of n_s, while for the boundary condition (7b) $\nu \equiv \nu(n_s)$, and (19) below becomes the transcendental equation for the determination of n_s (or b_s).

If one substitutes l_k and l from (14) and (15) into (16) (assuming stationarity), and excludes I_s using (18); (16) can be viewed as an (implicit) dependence of surface velocity on surface temperature:

$$\nu^2(\nu - C) = B \,, \quad C = \frac{L(1-n_s)k_s}{\alpha(H_s + L n_s)} \,, \tag{19}$$

$$B = \left(\frac{k_s}{b_s}\right)^2 \frac{\pi T_s}{2T_a} \times \frac{T_s K_s}{\alpha(H_s + L n_s)} \,.$$

The solution of this cubic equation exhibits Arrhenius-type behavior as a function of surface temperature T_s (Fig. 3b). To explain the observed change in activation energy, we divide both sides by C^3 and obtain two limiting cases:

$$B/C^3 \ll 1 \,, \quad \nu \approx C \,, \quad B/C^3 \gg 1 \,, \quad \nu \approx B^{1/3} \,. \tag{20}$$

The turnover between these two approximations occurs with $B \approx C^3$ i.e., with

$$I \approx I_1 \equiv \frac{\pi T_s}{2 b_s^2 T_a} \left(\frac{H_s + L n_s}{L(1-n_s)}\right)^2 T_s K_s \alpha \,. \tag{21}$$

In both cases the result (20) can be written in a form similar to surface formula (2) with re-normalized activation energy and pre-exponential factor.

$$\nu = \nu_0' \exp(-T_a'/T_s) \,, \tag{22a}$$

$$T_a' \equiv \frac{2}{3} T_a \,, \quad \nu_0' \equiv \left[\frac{\pi k_0^2 T_s}{2 b_s^2 T_a} \times \frac{T_s K_s}{\alpha(H_s + L n_s)}\right]^{1/3} \,, \quad I_s \ll I_1 \,, \tag{22b}$$

$$T_a' \equiv T_a \,, \quad \nu_0' \equiv \frac{k_0 L(1-n_s)}{\alpha(H_s + L n_s)} \,, \quad I_s \gg 1 \,. \tag{22c}$$

One can calculate T_s and ν from (18), (22) in the same way as for the surface model with volumetric enthalpy of ablation

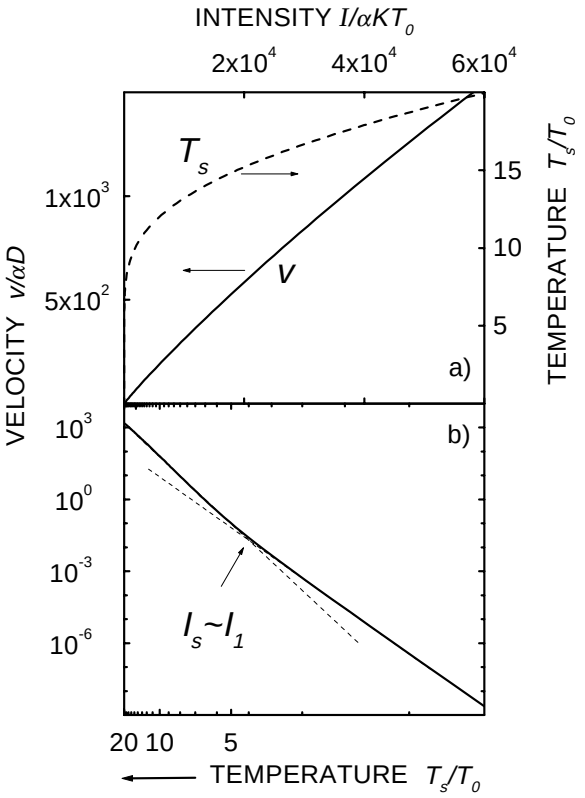

Fig. 3a,b. Parameters of stationary ablation for thermal volume decomposition model. Normalized variables are used for convenience. Parameters are given in Table 1. **a** Dependence of stationary velocity (*solid curve*) and surface temperature (*dashed curve*) on absorbed intensity. **b** Dependence of stationary velocity on surface temperature in Arrhenius coordinates: $\ln(\nu)$ vs. reciprocal temperature. Effective activation temperature for equivalent surface reaction changes from $2/3 T_a$ at low intensities to T_a at high intensities. This turnover can be seen only at the Arrhenius plot, near $T_s/T_0 \approx 4$

Ln_{cr} [39]. In [27] $L = 0$ was considered, $I_1 = \infty$, and only the case (22b) was relevant. The dependence of velocity on intensity is almost linear in all intensity range (Fig. 3a). The dependence $T_s(I_s)$ is logarithmic, due to the Arrhenius exponent in (22a). For estimations we assume $n_s \sim b_s \sim 0.5$, $H_s \sim Ln_s$, $T_s/T_a \sim 0.1 \Rightarrow I_1 \sim 3T_sK\alpha$ and typical turnover intensities I_1 for strongly absorbing polymers are some MW/cm^2. In order to compare v_0' in (22) with v_0 in surface models (2), we assume that (the upper limit of) k_0 in (6) is of the order of attempt frequency, $k_0 \sim 10^{13}$ s^{-1}. Factor v_0 in (2) is of the order of sound velocity [38], $v_0 \sim 10^6$ cm/s. For two cases in (22),

$$v_0' \sim \left(\frac{k_0^2 D}{\alpha}\right)^{1/3} \sim 10^6 \text{ cm/s}\,, \quad v_0' \sim k_0/\alpha \sim 10^8 \text{ cm/s}\,. \quad (23)$$

Here the values typical for strongly absorbing polymers have been assumed: thermal diffusivity $D \sim 10^{-3}$ cm^2/s, $\alpha \sim 10^5$ cm^{-1}. For weakly absorbing polymers these coefficients can be 10–10^3 times larger.

For generality, Figs. 3, 4, 6, 7 are plotted in dimensionless variables. Possible dimensional values of parameters, which are consistent with these figures are given in Table 1 together with parameters used in the calculations for PI.

One can see that for the stationary regime the surface evaporation model resembles the model under study in several respects. It is not, however, its limiting case. In particular, it can be shown that in the volume model maximum of temperature is always reached at the surface. Instead of formation of subsurface temperature maximum observed in surface

Table 1. Parameters used in calculations

Parameter	Dimensionless calculations	PI Kapton^{TM} H $\lambda = 248$ nm	References, notes (for PI)
Absorptivity A_s	1	0.9	[55]
Absorption coefficient α cm/s	10^5	3.2×10^5	[55]
Screening coefficient α_g cm/s in $I_s(t) = A_s I_0(t) \exp(-\alpha_g h(t))$	0	0.4α	Fitting, [31]
Thermal conductivity K W/cm K	10^{-2}	$1.55 \times 10^{-3}(T/T_0)^{0.28}$	Power fit to data [56, 57]
Specific heat c J/g K	1	$2.55 - 1.59\times$ $\times \exp[(T_0 - T)/460]$	Fit to data [56, 57], which saturates with T
Density ρ g/cm^3	1	1.42	[57]
Thermal diffusivity D cm^2/s	10^{-2}	$K/c\rho$	[56, 57]
Ambient temperature T_0 K	300	300	
Activation energy T_a K	$21\,000 \equiv 1.81$ eV	$17400 \equiv 1.5$ eV	[46, 49, 50]
Volume pre-exponential k_0 s^{-1}	10^{13}	2.67×10^{12}	Fitting parameter
Surface pre-exponential v_0 cm/s	10^8		
Critical fraction of broken bonds n_{cr}	0.5	0.9	Conjectured from [48]
Volumetric reaction enthalpy $L = \Delta H_b N_0$ J/cm^3	0 1.2×10^4 (Fig. 3)	2×10^3	Calculated from ΔH_b and N_0 below
Reaction enthalpy per bond ΔH_b eV	$1.5 \equiv 17\,400$ K	1.4	$\Delta H_b \le k_B T_a$ see above for T_a
Number density of bonds N_0 cm^{-3}	5×10^{22}	8.95×10^{21}	≈ 4 per monomer; [12] and Fig. 9
Mass fraction in the volatile species m_v/m_t	0.5	0.47	[12, 46, 47]
Laser pulse profile $I(t)$	$I_0 t/\tau \exp(-t/\tau)$	Triangular, I_{max} at $t = 0.66 t_{FWHM}$	
Laser pulse duration τ s	10^{-8}	15×10^{-9} (FWHM)	
One unit of dimensionless variable is			
Time $t^* = \alpha^2 Dt$	10^{-8}s		
Distance $h^* = \alpha h$, $x^* = \alpha x$	10^{-5}cm		
Velocity $v^* = v/\alpha D$	10^3cm/s		
Temperature $T^* = T/T_0$	300 K		
Intensity $I^* = I/\alpha K T_0$	0.3×10^6 W/cm^2		
Fluence $\phi^* = \phi\alpha/c\rho T_0$	3×10^{-3} J/cm^2		
Dimensionless combinations			
$\alpha^2 D\tau$	1		
Surface model $v_0/D\alpha$	10^5		
Volume model $k_0/D\alpha^2$	10^5		
T_a/T_0	70		
$L/c\rho T_0$	40		

models [39], the temperature distribution near the surface flattens off. As a result one can subdivide the x axis into two regions. In the reaction region, absorbed energy goes into the enthalpy of decomposition reaction. In the conduction region reaction rate is small and absorption is balanced by changes in temperature. The size of reaction region (for high velocities) is of the order of $1/\alpha$.

3 Transient regimes

Stationary regimes described in the previous section are seldom reached in ns laser pulses. Besides, they cannot explain near-threshold behavior. For this reason we now consider non-stationary regimes, such as approach to a stationary solution and regimes with the time-dependent intensity. With high fluences screening effects determine the ablation rate for almost any ablation mechanism [26, 31], whereas near-threshold shielding is negligible. Therefore, to discriminate between different ablation models one has to study near-threshold behavior. We will assume constant material parameters, zero ablation enthalpy $L = 0$, and Stefan-type condition (7a), as this allows us to derive analytical results and to perceive distinctions from the surface models. Consideration of the temperature-dependent parameters usually does not lead to new qualitative effects, though it can change the numbers significantly.

3.1 Onset of ablation in Stefan-type problem

Let us consider the laser pulse with $\phi > \phi_{\rm th}$. A critical fraction of broken bonds near the surface, $n_{\rm cr}$ is produced at a moment of time $t_{\rm cr}$ (Fig. 4a).

Before the movement of the front starts, the profile of broken bonds $n_{\rm b}$ (or b in (11)) is parabolic near $x = 0$, (Fig. 5, $t < t_{\rm cr}$), because temperature $T(x)$ and reaction rate $k(T(x))$ have zero derivative at the surface. Thus, at $t = t_{\rm cr}$:

$$b(x) \approx b_{\rm cr} + b''(x=0)\frac{x^2}{2}\,. \tag{24}$$

Here prime stands for spatial derivative. After the onset of ablation $n_{\rm b}$ (and b) continue to increase within the volume, and the position of the front in the laboratory system "slides" over the pre-created $n_{\rm b}$ profile, in a way that keeps $n_{\rm s} \equiv n_{\rm cr} =$ constant (Fig. 5).

Let us estimate the time $\Delta t = t - t_{\rm cr}$ in which ablation front arrives at the point x. At the point x, b increases with the rate $\dot{b}(x=0, t_{\rm cr})$ (dot stands for time derivative). This is valid with the accuracy about Δt and x^2, as follows from Taylor expansion. Thus, the time needed for $b(x)$ to reach $b_{\rm cr}$ is:

$$\Delta t = -\frac{b''(x=0, t_{\rm cr})x^2}{2\dot{b}(x=0, t_{\rm cr})}\,. \tag{25}$$

This yields the dependence of ablated depth $h \equiv x$ on time near onset of ablation. Because $v \equiv 0$ for $t < t_{\rm cr}$, the denominator can be immediately calculated from (12). The numerator can be found by integrating the second spatial derivative of

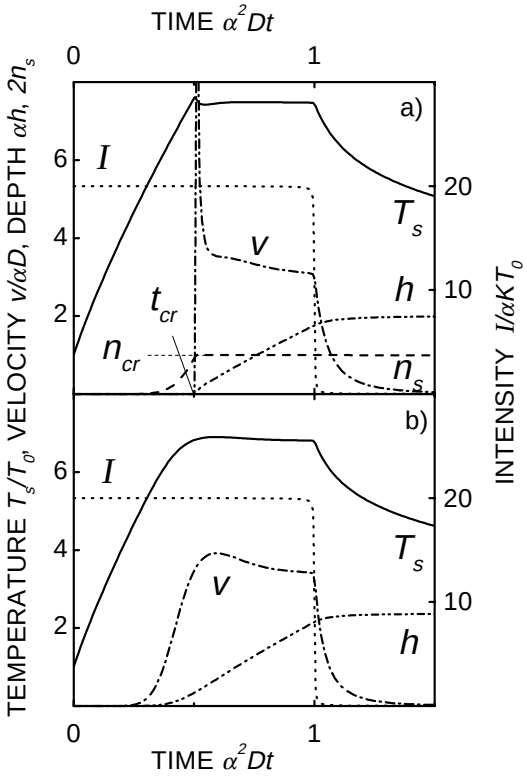

Fig. 4a,b. Onset of ablation for volume and surface models with constant intensity (*dotted curve*) $I/\alpha K T_0 = 20$. Other parameters are given in Table 1. Surface temperature $T_{\rm s}$ - *solid curve*, fraction of broken bonds at the surface $n_{\rm s}$ - *dashed curve*, recession velocity v - *dash-dot*, and ablated depth h - *dash-double dot*. **a** Volume model. Ablation starts sharply, at $t_{\rm cr}$ when $n_{\rm cr}$ is reached at the surface. Ablated depth has a square-root behavior. Velocity v is singular near onset and approaches stationary value from above. Surface temperature stabilizes very fast. **b** Surface model. Smooth ablation onset, velocity remains always finite

(12) within approximation (13):

$$h(t) = A(t - t_{\rm cr})^{1/2}\,, \quad A = \left[k_{\rm s}(t_{\rm cr}) \Big/ \int_0^{t_{\rm cr}} \frac{k_{\rm s}(t')}{l_k^2(t')}\,{\rm d}t' \right]^{1/2}\,. \tag{26}$$

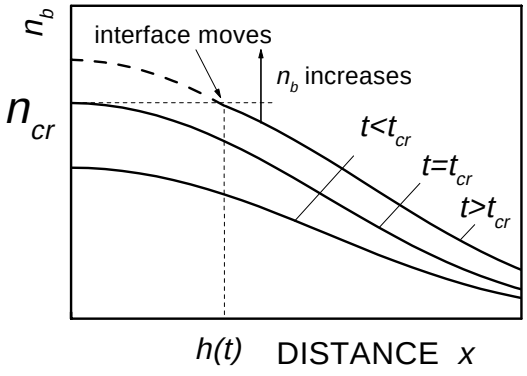

Fig. 5. Distribution of the broken bonds within the material. Before the start of ablation ($t < t_{\rm cr}$), the profile is parabolic near the surface, which leads to an explosive onset of ablation at $t = t_{\rm cr}$. As interface moves ($t > t_{\rm cr}$), finite slope of $n_{\rm b}(x)$ near the surface is formed self-consistently

This holds as long as $h \ll l_k$, and

$$t - t_{\rm cr} \ll k_{\rm s}/\dot{k}_{\rm s} \approx T_{\rm s}^2/T_{\rm a}\dot{T}_{\rm s} \,. \tag{27}$$

Square-root dependence of $h(t)$ in (26) leads to an infinite velocity at the initial moment (explosive onset of ablation):

$$v = \frac{A}{2(t-t_{\rm cr})^{1/2}} \,. \tag{28}$$

The derivative $\partial n_{\rm b}/\partial x(x=0) \neq 0$ anymore, but becomes negative, and, finally (for the constant intensity) approaches its stationary value (Fig. 5, $t > t_{\rm cr}$).

Figure 4 shows differences in the onset of ablation in the volume model (upper part) and surface model (lower part). Parameters are when possible identical and listed in Table 1. Initial heating stages are similar. In the volume model ablation starts sharply and the velocity is initially singular. (In reality velocity is restricted by physical constrains, for example, by the sound velocity). Such an "explosion" may be responsible for the acoustic signal, which was frequently used to determine ablation onset [7, 43]. In the surface model ablation starts earlier in an Arrhenius-type fashion and velocity does not significantly exceed its stationary value. The differences are most pronounced near the onset. In the later stages both models predict similar quasi-stationary regimes.

For the case depicted in Fig. 4, the surface temperature at the onset of ablation increases. Assuming that l_k in (26) is a slow function in comparison with $k_{\rm s}$, and using the saddle-point method near $t = t_{\rm cr}$, one obtains with l_k from (14):

$$\begin{aligned} A &\approx \left(\frac{T_{\rm a}\dot{T}_{\rm s}}{T_{\rm s}^2}\right)^{1/2} l_k\Big|_{t=t_{\rm cr}} = \left(\frac{2D_{\rm s}}{\alpha I_{\rm s}/c_{\rm s}\rho\dot{T}_{\rm s} - 1}\right)^{1/2}\Bigg|_{t=t_{\rm cr}} \\ &= \left(\frac{2D}{{\rm e}^{-\alpha^2 D t_{\rm cr}}/{\rm erfc}\sqrt{\alpha^2 D t_{\rm cr}} - 1}\right)^{1/2} . \end{aligned} \tag{29}$$

The second equality was obtained using (14), (15) (with $L = 0$). The third equality refers to the constant parameters and laser intensity. $A \to \infty$ if heat conduction can be neglected (denominator in (29) equals zero in this case). With heat conduction, $\dot{T}_{\rm s}$ is lower, $t_{\rm cr}$ increases, while A decreases. With very strong heat conduction $A \to 0$. Explicitly, A is almost independent on kinetic parameters k_0 and $T_{\rm a}$, or on the intensity. It is determined rather by the profile and duration of the laser pulse. A does however depend on them implicitly, via $t_{\rm cr}$. Using a saddle-point approximation (i.e., assuming that the majority of bonds are broken just before $t_{\rm cr}$), we obtain from (12):

$$b_{\rm cr} = \int_0^{t_{\rm cr}} k_{\rm s}(t)\,{\rm d}t = k_{\rm s}\frac{T_{\rm s}^2}{T_{\rm a}\dot{T}_{\rm s}}\bigg|_{t=t_{\rm cr}} . \tag{30}$$

For constant parameters estimation from below can be obtained neglecting heat conduction (this is realistic for polymers in the initial stage of heating):

$$t_{\rm cr} > \frac{c\rho T_{\rm a}}{\alpha I_{\rm s}} \Big/ \ln\left[\frac{c\rho T_{\rm a}}{\alpha I_{\rm s}}\frac{k_0}{b_{\rm cr}}\right] . \tag{31}$$

3.2 Behavior of the surface temperature near the onset of ablation

With $t > t_{\rm cr}$, $T_{\rm s}$ will increase slower, or even decrease, due to the movement of the ablation front. The Green function of the (linear) heat equation (4) can be obtained for arbitrary $v(t) \equiv \partial h/\partial t$. Its Taylor expansion for small h yields for the surface temperature immediately after the onset of ablation

$$T_{\rm s} \approx T_{\rm s}(h \equiv 0) + \frac{h^2}{2}\frac{\partial^2 T}{\partial x^2}(h \equiv 0, x = 0, t = t_{\rm cr}) \,. \tag{32}$$

$T(h \equiv 0)$ refers to the case without interface movement. Thus, near $\phi_{\rm th}$, changes in $T_{\rm s}$ are only due to changes in the position of the front in the laboratory frame – the interface penetrates the temperature distribution created before ablation. With square-root behavior of ablated depth near $t = t_{\rm cr}$ in (26) this predicts a jump in the time derivative $\dot{T}_{\rm s}$ immediately after $t_{\rm cr}$. With $\partial^2 T/\partial x^2$ from (15) (with $L = 0$):

$$\dot{T}_{\rm s} = \dot{T}_{\rm s}(h \equiv 0, t_{\rm cr}) + \frac{A^2}{2D_{\rm s}}\left(\dot{T}_{\rm s}(h \equiv 0, t_{\rm cr})\right) - \frac{\alpha I_{\rm s}(t_{\rm cr})}{c_{\rm s}\rho} \,. \tag{33}$$

With A from (29) the resulting time derivative is equal zero, i.e., $T_{\rm s} \approx$ const. in (32). This explains why $T_{\rm s}$ stabilizes quickly (Fig. 4). It has the tendency to remain constant even for $I(t) \neq$ constant.

4 Near-threshold behavior for short pulses

Differences between the volume and the surface model are even more pronounced for near-threshold ablation by short pulses with variable intensity. With volume mechanism broken bonds are accumulated within the bulk during the time when the material is hot. Thus, thermal history of the specimen becomes important. With $\phi \approx \phi_{\rm th}$, ablation starts after the laser pulse and after the maximum temperature $T_{\rm m}$ is reached at $t = t_{\rm m}$ (Fig. 6a). Formally, with $\phi \to \phi_{\rm th} + 0$, the burst of ablation occurs at $t \to \infty$. With surface model (Fig. 6b) the onset of ablation is smooth, the maximum of ablation velocity coincides with the maximum of surface temperature, and the velocity remains always small. For volume model, despite small total ablated depth, the maximum value of velocity is very big (singular) even near the threshold.

Let us discuss the fluence dependence of the single-pulse near-threshold total ablated depth and the value of threshold fluence. Near the threshold, ablation does not influence the temperature and the reaction rate. Therefore, one can assume, that the profile $b(x)$, which is parabolic near $x = 0$,

$$b(x) \approx (b_{\rm cr} + \Delta b)\left(1 - x^2/l_k^2(t_{\rm m})\right) \tag{34}$$

is created near $t \approx t_{\rm m}$ when the reaction rate has a sharp maximum. Afterwards, all material with $b(x) > b_{\rm cr}$ is ablated. Therefore total ablated depth per pulse $h(t = \infty)$ is:

$$h(\infty) \approx \left[\frac{\Delta b}{b_{\rm cr}}\right]^{1/2} l_k(t_{\rm m}) \,. \tag{35}$$

To relate $h(\infty)$ to the parameters of the laser pulse, we apply the saddle-point method near $t_{\rm m}$:

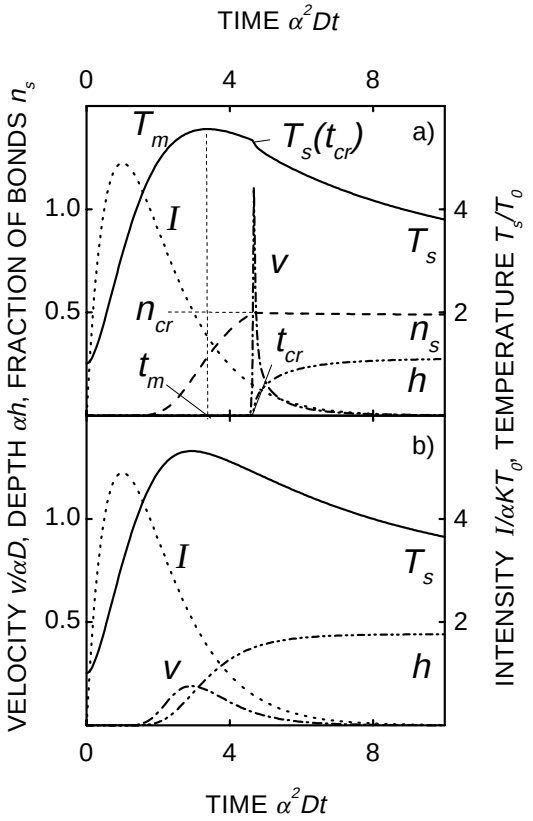

Fig. 6a,b. Near threshold ablation with smooth laser pulse for volume and surface models. $\phi\alpha/c\rho T_0 = 13.3$, other parameters are given in Table 1. Surface temperature T_s - *solid curve*, fraction of broken bonds at the surface n_s - *dashed curve*, recession velocity v - *dash-dot*, and ablated depth h - *dash-double dot*. **a** Volume model. Ablation occurs after the pulse and after the maximum surface temperature T_m was reached at t_m. Despite small total ablated depth, ablation velocity is very high. **b** Surface model. Maximum of velocity corresponds to maximum in surface temperature and velocity is small near the threshold

$$b_{cr} + \Delta b = \int_0^\infty k_s(t)\,dt \approx \left[\left(\frac{2\pi T_s^2}{-\ddot{T}_s T_a}\right)^{1/2} k_s\right]\Bigg|_{t=t_m} . \qquad (36)$$

At threshold one should set $\Delta b = 0$, find the maximum temperature $T_m(t = t_m)$ and recalculate it into threshold fluence using heat equation. As $h(\infty) \propto \Delta b^{1/2}$ in (35), and $b_{cr} + \Delta b$ in (36) increases linearly with $\phi - \phi_{th}$ (in the first order), h has a square-root dependence on $\phi - \phi_{th}$. With constant parameters, and $T_0 \ll T_m$,

$$h(\infty) \approx \frac{1}{\alpha}\left[\frac{2\theta_m I_0}{I_m}\right]^{1/2}\left(\frac{\phi-\phi_{th}}{\phi_{th}}\right)^{1/2},$$
$$\phi_{th} \approx \frac{c\rho T_a}{A_s\alpha}\left[\frac{\tau^*}{\theta_m \ln\left[y/\sqrt{\ln y}\right]}\right], \quad y = \frac{k_0}{b_{cr} D\alpha^2}\left[\frac{2\pi\theta_m}{-\ddot{\theta}_m}\right]^{1/2}, \qquad (37)$$

$\tau^* = D\alpha^2\tau$ is the dimensionless pulse duration, $\theta(t^*) \equiv I_0^{-1}\int_0^{t^*} e^{t^*-t_1^*}\mathrm{erfc}\sqrt{t^*-t_1^*}\,I(t_1^*)\,dt_1^*$ the dimensionless temperature, and A_s the absorptivity. I_0 and τ are defined in such a way that $\phi = I_0\tau$. The (dimensionless) expressions in square brackets can be calculated for a given temporal profile of the pulse.

5 Ablation curves: depletion of species and real ablation

One of the main motivations for the development of the volume thermal model was the observation of a *sharp* onset of ablation in profile measurements and *smooth* threshold in mass loss studies. The preceding discussion shows that volume decomposition model results in a sharp onset of ablation. This, in contrast to the behavior expected for a purely surface process, explains the first part of experimental observations.

Arrhenius tails are observed on polymers in mass loss measurements near ϕ_{th} [8]. This does not contradict the present model, as the aforementioned results refer to a layer-by-layer material removal and crater formation, revealed in profile measurements. The contradiction disappears, if we assume that the tails are due to a sub-threshold degradation of polymer. In a previous paper [44] we considered two different processes: the creation of volatile species and their depletion from the volume, and surface ablation. Within the present picture both processes result from the same bulk reaction. It breaks the bonds, destroys polymer chains, and may simultaneously create trapped volatile species (Fig. 2).

With $\phi < \phi_{th}$, all volatile fragments result in a mass loss, which requires out-diffusion of trapped species and occurs on the μs or even ms time scale. As volatile species and broken bonds are produced in a pyrolytic reaction (6), this results in an Arrhenius tail. With $\phi > \phi_{th}$, volatile species leave the material together with the ablation products. When ablation ceases ($n_b(x = 0) < n_{cr}$) some of the volatile species still exist below the surface and leave the material later. This results in an additional mass loss, M (per unit area), which does not contribute to the ablated (crater) depth. M, which is due to the depletion of species, is proportional to the number of broken bonds left within the material after ablation, i.e., at the time $t = t_{\text{end of ablation}}$. Because these species do not diffuse on the ns time scale, their spatial distribution repeats that of the broken bonds and can be calculated as:

$$M = m_v N_0 \int_0^\infty n_b(x)\,dx\,, \quad h_M \equiv \frac{M}{\rho} = \frac{m_v}{m_t}\int_0^\infty n_b(x)\,dx\,. \qquad (38)$$

N_0 is the total concentration of virgin bonds, and m_v the mass of volatile products produced per broken bond. m_v/m_t is the mass fraction, related to volatile species (per bond). It depends on the chemistry of the process, but it is always less than one (for PI it is about 0.5 [12]). In previous investigations the ablated depth was calculated from the total mass loss $h\rho + M$. This is erroneous, because the depletion of species may take place without any change in the surface profile. In order to compare the predictions of the model with such measurements, we introduced the "depth" h_M related to M, and also the total effective "depth" $h + h_M$.

The dependence of h_M on fluence is shown in Fig. 7 by the dashed line. Below threshold, an Arrhenius-type behavior is found. At high fluences, h_M becomes almost constant; it has a sharp maximum near ϕ_{th}. This is because above the threshold, the modified region, left after the ablation ceases, is smaller than the modified region for near threshold fluences. Figure 8 illustrates the matters. Before the start of real ablation, distribution of n_b and of volatile species is parabolic near the surface, i.e., rather wide. As ablation front moves, the smooth top of this distribution ablates together

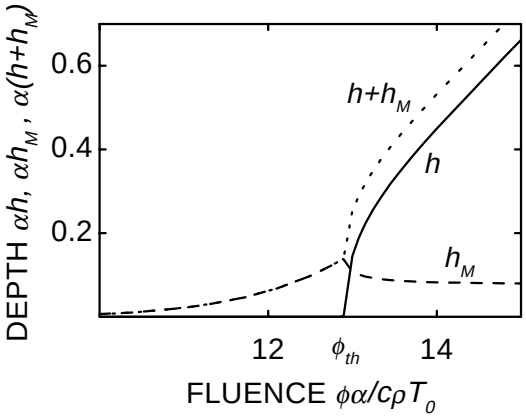

Fig. 7. Contributions of mass loss via volatile species h_M (*dashed line*) and real ablation h (*solid line*) to the overall effective ablated depth $h_t = h_M + h$ (*dotted line*). Arrhenius tails below threshold are due to volatile species. In this region *dashed* and *dotted lines* coincide. Real ablation starts sharply. Modification of material and loss of volatile species h_M have a sharp maximum near ϕ_{th}

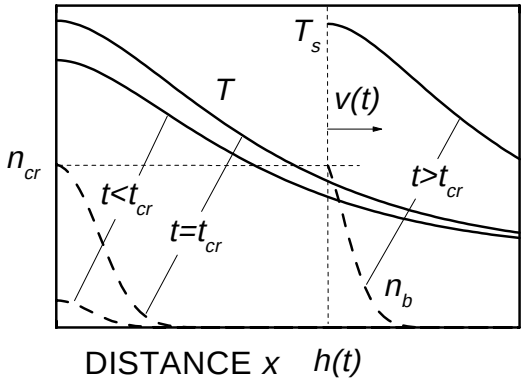

Fig. 8. Schematic, that explains the maximum of subsurface modification near threshold shown in Fig. 7. When ablation starts, volatile species are ablated together with the material; $n_{\text{b}}(x)$ distribution becomes more steep and the total number of broken bonds (and volatile species) under the surface decreases. See also Fig. 5

with the material. Distribution, which is left after the ablation, is not parabolic. It is narrower, which decreases its contribution to the depletion-related mass loss. An increase in surface modification around ϕ_{th} was observed in conductivity measurements [45].

The total effective ablated depth (dotted line) is monotonous with fluence, but may exhibit an inflection point or singularity in slope. Such a behavior, reported, for example, in [8] is inherent in the present model, and does not require additional mechanisms related to the screening of the incoming radiation, and is due to the square root dependence of real ablation on fluence near ϕ_{th}.

6 Example: single-pulse ablation of polyimide

To estimate the differences between the mass-loss and profile measurements predicted by the theory, we consider single-pulse ablation of polyimide (PI). It is known, that PI can lose up to 50% of its weight in thermal degradation; The polymer chain destroys mainly via the breaking of imide rings [12],

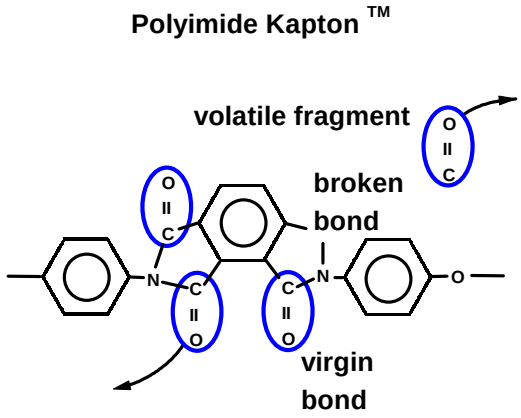

Fig. 9. Monomer of Polyimide Kapton™ H. Carbonyl groups constitute the majority of volatile species for PI and their cleavage produces broken bonds

primary lost species being CO molecules [46, 47] (Fig. 9). This is in agreement with mass spectrometry (QMS) performed for ns laser pulses [48]. Activation energies for the degradation of PI are about 1.5 eV [46, 49, 50], This agrees well with the analysis of ablation data on the basis of a purely thermal surface models for ns [26] and μs pulses [25, 29].

Figure 10 shows the modeling of the single-pulse ablation of PI. Experimental points are taken from [8]. In calculations we used the (modified) code developed in our previous work [25, 33, 44, 51] as well as the method of moments designed for similar problems [26]. Parameters are listed in Table 1. The picture demonstrates all characteristic features revealed by Fig. 7. The singularity in slope observed near ϕ_{th} is smoothened if boundary condition (7b) or more realistic conditions are used. Threshold for real ablation lies higher than the value that follows from the linear or logarithmic fit of ablation curve. The theory predicts discrepancy between mass-loss and profile measurements of the order of 10 nm near ϕ_{th}. The decrease of ablation rate at high fluences re-

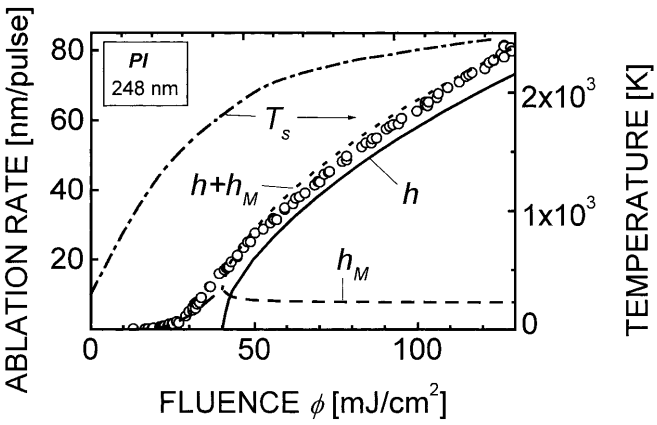

Fig. 10. Experimental [8] and theoretical curves of PI ablation for KrF laser. Parameters used in calculations are listed in Table 1. Mass loss via volatile species h_M (*dashed line*), real ablation h (*solid line*), overall effective ablated depth $h_t = h_M + h$ (*dotted line*). Calculated maximum surface temperature T_{s} (*dash-dotted line*) saturates when real ablation starts. If movement of the boundary due to ablation is neglected, T_{s} reaches unrealistic temperatures $\sim 5 \times 10^3$ K as in [24]. Arrhenius tails are due to volatile species, real ablation starts sharply. The theory predicts that near the threshold of real ablation the difference between mass-loss and profile measurements is about 10–20 nm

quires the consideration of screening. However the absorption coefficient of ablated products α_g is smaller than in the previous analysis [26, 33], as initial decrease in the slope of the ablation curve is due to the square-root behavior (37).

The obtained fit is to a certain degree ambiguous. Namely, with higher values of n_{cr}, the threshold fluence for the real ablation will increase. One can obtain another fit with comparable accuracy by simultaneously changing the values of L and m_v/m_t (and α_g). Thus, the picture should rather serve as a guideline for the experiments, which target to determine the discrepancy between the mass-loss and profile measurements in single-pulse ablation. There exists an inherent difficulty in this type of experiments near the threshold. AFM works best with small areas, where the mass loss is undetectable, whereas QCM requires big ablated areas inconvenient for the profile analysis by the AFM due to large-scale roughness of the material.

Moreover, the mass loss from the bulk of material may influence the surface morphology even below threshold. In polymers with flexible chains such as PMMA, this may result in essential decrease of thickness of thin polymer film due to free volume relaxation [52]. In polymers with hard chains such as PI this relaxation should be hindered. On the other hand, with PI such phenomena as "hump" and "dent" formation are observed [53]. They impede the AFM measurements of ablation kinetics near the threshold.

The loss of volatile species and subsequent recombination of radicals may lead to a carbonization [9] of the material and a second threshold in multiple-pulse ablation [48, 54]. We suggested an explanation of this effect on the basis of competition between the ablation and carbonization [27].

7 Conclusions

It is shown, that bulk photothermal degradation of polymers under the action of laser light may result in ablation. The developed model differs in several respects from the surface models. It predicts a sharp (explosive) ablation threshold and the differences in ablation rates measured by profilometry and mass loss (about 10 nm for PI). Near-threshold ablation occurs significantly after the end of the laser pulse, and has high values of ablation velocity, despite small ablated depth per pulse. A similar theoretical approach can be applied to HTSC, oxidic (ferroelectric) perovskites, and other materials, where a depletion of species for fluences $\phi \leq \phi_{th}$ is observed [3]. A more detailed comparison with the experimental results requires the consideration of backward and/or subsequent chemical transformations, changes in material properties, etc.

Acknowledgements. We wish to thank Prof. D. Bäuerle for valuable discussions. This work was supported by the "Jubiläumsfonds der österreichischen Nationalbank" project #7563 and the "Russian Foundation for Basic Researches".

References

1. R. Srinivasan, V. Mayne-Banton: Appl. Phys. Lett. **41**, 576 (1982)
2. Y. Kawamura, K. Toyoda, S. Namba: Appl. Phys. Lett. **40**, 374 (1982)
3. D. Bäuerle: *Laser Processing and Chemistry*, 2nd edn. (Springer, Berlin, Heidelberg 1996)
4. S.V. Babu, G.C. D'Couto, F.D. Egitto: J. Appl. Phys. **72**(2), 692 (1992)
5. M. Himmelbauer, E. Arenholz, D. Bäuerle: Appl. Phys. A **63**, 87 (1996)
6. G. Paraskevopoulos, D.L. Singleton, R.S. Irwin, R.S. Taylor: J. Appl. Phys. **70**, 1938 (1991)
7. R.S. Taylor, D.L. Singleton, G. Paraskevopoulos: Appl. Phys. Lett. **50**(25), 1779 (1987)
8. S. Küper, J. Brannon, K. Brannon: Appl. Phys. A **56**, 43 (1993)
9. M. Schumann, R. Sauerbrey, M. Smayling: Appl. Phys. Lett. **58**, 428 (1991)
10. Z. Ball, B. Hopp, M. Csete, F. Ignácz, B. Rácz, R. Sauerbrey, G. Szabó: Appl. Phys. A **61**, 547 (1995)
11. Z. Ball, B. Hopp, M. Csete, F. Ignácz, B. Rácz, G. Szabó, R. Sauerbrey: Appl. Phys. A **61**, 575 (1995)
12. R. Srinivasan, R.R. Hall, W.D. Loehle, W.D. Wilson, D.C. Allbee: J. Appl. Phys. **78**, 4881 (1995)
13. J. Lu, S.V. Deshpande, E. Gulari, J. Kanicki, W.L. Warren: J. Appl. Phys. **80**(9), 5028 (1996)
14. J.E. Andrew, P.E. Dyer, D. Forster, P.H. Key: Appl. Phys. Lett. **43**, 717 (1983)
15. T.F. Deutsch, M.W. Geis: J. Appl. Phys. **54**, 7201 (1983)
16. H.H.G. Jellinek, R. Srinivasan: J. Phys. Chem. **88**, 3048 (1984)
17. E. Sutcliffe, R. Srinivasan: J. Appl. Phys. **60**, 3315 (1986)
18. S. Lazare, V. Granier: Laser Chem. **10**, 25 (1989)
19. G.D. Mahan, H.S. Cole, Y.S. Liu, H.R. Philipp: Appl. Phys. Lett. **53**(24), 2377 (1988)
20. G.C. D'Couto, S.V. Babu: J. Appl. Phys. **76**(5), 3052 (1994)
21. S.R. Cain, F.C. Burns, C.E. Otis: J. Appl. Phys. **71**(9), 4107 (1992)
22. S.R. Cain, F.C. Burns, C.E. Otis, B. Braren: J. Appl. Phys. **72**, 5172 (1993)
23. D. Bäuerle, B. Luk'yanchuk, P. Schwab, X.Z. Wang, E. Arenholz: In *Laser Ablation of Electronic Materials*, ed. by E. Fogarassy, S. Lazare, E-MRS 4 (North Holland-Elsevier 1992) p. 39
24. S. Cain: J. Phys. Chem. **97**, 7572 (1993)
25. B. Luk'yanchuk, N. Bityurin, M. Himmelbauer, N. Arnold: Nucl. Instrum. Meth. B **122**, 347 (1997)
26. N. Arnold, B. Luk'yanchuk, N. Bityurin: Appl. Surf. Sci. **127**, 184 (1998)
27. N. Bityurin, N. Arnold, B. Luk'yanchuk, D. Bäuerle: Appl. Surf. Sci. **127**, 164 (1998)
28. F.C. Burns, S.R. Cain: J. Phys. D **29**, 1349 (1996)
29. K. Piglmayer, E. Arenholz, K. Ortwein, N. Arnold, D. Bäuerle: Appl. Phys. Lett. **73**(6), 847 (1998)
30. V. Srinivasan, M.A. Smrtic, S.V. Babu: J. Appl. Phys. **59**(11), 3861 (1986)
31. H. Schmidt, J. Ihlemann, B. Wolff-Rottke, K. Luther, J. Troe: J. Appl. Phys. **83**(10), 5458 (1998)
32. B. Luk'yanchuk, N. Bityurin, S. Anisimov, D. Bäuerle: Appl. Phys. A **57**, 367 (1993)
33. B. Luk'yanchuk, N. Bityurin, S. Anisimov, N. Arnold, D. Bäuerle: Appl. Phys. A. **62**, 397 (1996)
34. N. Bityurin, A. Malyshev, B. Luk'yanchuk, S. Anisimov, D. Bäuerle: Proc. SPIE **2802**, 103 (1996)
35. N. Bityurin: Appl. Surf. Sci. **138-139**, 354 (1999)
36. R. Srinivasan, B. Braren: Chem. Rev. **89**, 1303 (1989)
37. G.V. Treyz, R. Scarmozzino, R.M. Osgood, Jr.: Appl. Phys. Lett. **55**(4), 346 (1989)
38. S.I. Anisimov, Y.A. Imas, G.S. Romanov, Y.V. Khodyko: *Action of High-Power Radiation on Metals* (National Technical Information Service, Springfield, Virginia 1971)
39. S.I. Anisimov, V.A. Khokhlov: *Instabilities in Laser-Matter Interaction*, (CRC Press, Boca Raton 1995)
40. V.N. Tokarev, J.G. Lunney, W. Marine, M. Sentis: J. Appl. Phys. **78**(2), 1241 (1995)
41. J.R. Sobehart: J. Appl. Phys. **74**(4), 2830 (1993)
42. J.K. Frisoli, Y. Hefetz, T.F. Deutsch: Appl. Phys. B **52**, 168 (1991)
43. P.E. Dyer, V. Srinivasan: Appl. Phys. Lett. **48**, 445 (1986)
44. M. Himmelbauer, N. Bityurin, B. Luk'yanchuk, N. Arnold, D. Bäuerle: Proc. SPIE **3093**, 224 (1997)
45. E. Arenholz, J. Heitz, M. Wagner, D. Bäuerle, H. Hibst, A. Hagemeyer: Appl. Surf. Sci. **69**, 16 (1993)
46. W.W. Wright: In *Developments in Polymer Degradation-3*, ed. by N. Grassie (Appl. Sci. Publisher, London 1981)
47. H.H. Jellinek (Ed.): *Aspects of Degradation and Stabilization of Polymers* (Elsevier, Amsterdam 1978) p. 278
48. S. Lazare, W. Guan, D. Drilhole: Appl. Surf. Sci. **96-98**, 605 (1996)

49. M.I. Bessonov: *Polyimides - a Class of Thermally Stable Polymers*, (NASA Technical Memorandum, Washington DC 20546 1986) p. 135
50. L.A. Laius, E.N. Dergacheva, T.J. Zhukova: In *Polyimides: Matrials: Chemistry and Characterization*, ed. by C. Feger, M.M. Khojasteh, J.E. McGrath, Proc. 3d Intl. Conf. on Polyimides (Elsevier, Amsterdam 1988) p. 389
51. N. Bityurin, A. Malyshev: Appl. Surf. Sci. **127-129**, 199 (1998)
52. N. Bityurin, S. Muraviov, A. Alexandrov, A. Malyshev: Appl. Surf. Sci. **110**, 270 (1997)
53. M. Himmelbauer, E. Arenholz, D. Bäuerle, K. Schichler: Appl. Phys. A **63**, 337 (1996)
54. Z. Ball, T. Feurer, D.L. Callahan, R. Sauerbrey: Appl. Phys. A **62**, 203 (1996)
55. E.T. Arakawa, M.W. Williams, J.C. Ashley, L.R. Painter: J. Appl. Phys. **52**, 3579 (1981)
56. G. Kotelnikov, A. Sidorovich: Polymer Sci. USSR **25**, 3053 (1983)
57. DuPont, Inc.: *Kapton Polyimide Film - Summary of Properties* (1988)